

Notice

This manuscript is a non-peer reviewed preprint submitted to EarthArXiv. It has been submitted for publication to GJI on 27/10/2020 with reference ID #GJI-20-1072. Newer versions may be moderately different with slight variations in content.

Manuscript details

Title: Future magnitude 7.5 earthquake offshore Martinique: Spotlight on major source-related factors of ground-motion variability

Authors: Elif ORAL (IPGP and Geoazur) and Claudio Satriano (IPGP)

Contact: elif.oral@geoazur.unice.fr

1 **Future magnitude 7.5 earthquake offshore Martinique:** 2 **Spotlight on major source-related factors of ground motion** 3 **variability**

4 Elif Oral^{1,2} and Claudio Satriano¹

¹ *Université de Paris, Institut de physique du globe de Paris, CNRS, F-75005 Paris, France*

² *Université Côte d'Azur, IRD, CNRS, Observatoire de la Côte d'Azur, Géoazur, France*

5 27 October 2020

6 **SUMMARY**

7 The eastern offshore of Martinique is one of the active areas of the Lesser Antilles Subduc-
8 tion Zone (LASZ). Although its seismicity is moderate compared to other subduction zones,
9 LASZ is capable of generating a M 7+ interplate earthquake and recent studies and historical
10 events, such as the M8 1839 and M 7-7.5 1946 earthquakes, confirm this possibility. Given
11 the high risk that Martinique can face in case of unpreparedness for such a M 7+ earthquake,
12 and the lack of a regional seismic hazard study, we investigated through numerical mod-
13 elling the ground motion variability for a hypothetical M_w 7.5 interplate earthquake. Our
14 main objective is to highlight the major factors related to earthquake source that can bring
15 the highest variability of ground motion at four broadband seismic stations across Mar-
16 tinique. For this purpose, we generated 320 rupture scenarios through a fractal kinematic
17 source model, by varying rupture directivity, source dimension, slip distribution. We com-
18 puted the broadband ground motion (0.5-25 Hz) by convolution of source-time functions
19 with Empirical Green's Functions (EGFs), that we selected from the analysis of moderate
20 events (M 4-4.5) recorded in the area of interest since 2016 by the West Indies network.
21 We found that the fault geometry and the spatial extension of the largest slip patch are the
22 most determinant source-related factors of ground motion variability. The significance of
23 such ground motion variability with respect to ground motion prediction equations (GM-

24 PEs) depends on the evaluated frequency of ground motion and on the station. Moreover,
25 we concluded that the EGF selection can be another significant factor of the variability of
26 the modelled ground motion depending on station. Our results provide a new insight on
27 the source-related ground-motion variability across Martinique and can guide future blind
28 seismic hazard assessment studies in different regions.

29 **Key words:** Strong ground motion, Fault slip, Rupture propagation, Source time functions,
30 Synthetic seismograms

31 1 INTRODUCTION

32 Martinique is located on the Lesser Antilles Subduction Zone (LASZ, Fig. 1), that is moderately
33 active but capable of generating a $M > 7$ interplate earthquake (e.g., [Feuillet et al. 2011](#)). LASZ
34 is formed by the subduction of the Atlantic oceanic lithosphere under the Caribbean plate at a
35 relatively slow convergence rate of 18 mm per year ([DeMets et al. 2010](#)). Martinique island is
36 part of the north-south trending magmatic arc of LASZ. The seismicity of LASZ can be divided
37 into: 1) flat-thrust interplate events above approximately 50 km in the fore-arc; 2) deep in-
38 traslab events in the back-arc; 3) intraplate events within the Caribbean Plate ([Russo et al. 1992](#);
39 [Laigle et al. 2013](#); [Ruiz et al. 2013](#)). The scarcity of large ($M > 7$) interplate thrust earthquakes
40 in LASZ implies an unusual strain release compared to other subduction zones ([Russo et al.](#)
41 [1992](#)). Nonetheless, past studies ([Ruiz et al. 2013](#); [Laigle et al. 2013](#); [Weil-Accardo et al. 2016](#))
42 proposed that LASZ has high potential to generate a mega-thrust earthquake: the seismogenic
43 zone might extend to the mantle wedge, below the forearc, and moderate seismic activity at
44 the base of the seismogenic zone can load shallower segments and initiate a larger mega-thrust
45 event. An example of this phenomenon was observed during the 2011 M_w 9 Tohoku, Japan
46 earthquake; [Laigle et al. \(2013\)](#) and [Satriano et al. \(2014\)](#) point to the similarities between the
47 North-Eastern Japan mega-thrust and LASZ—such as the lack of tremors and very-slow-low-
48 frequency earthquakes, and the sustained activity in the mantle wedge—to better understand the
49 long-term seismic activity of LASZ. Indeed, the recent study of [Paulatto et al. \(2017\)](#), linking
50 heterogeneity of V_p/V_s ratio to earthquake activity in LASZ, supports the proposed tectonic
51 explanation and the analogy between the North-Eastern Japan mega-thrust and LASZ.

52 Historical events in the region confirm the possibility of a mega-thrust earthquake genera-
53 tion in LASZ. [Feuillet et al. \(2011\)](#) compiled the data from several reports and papers for all
54 significant historical earthquakes in the Lesser Antilles. They concluded that the magnitudes of
55 the 1839 and the 1946 earthquakes offshore Martinique (Fig. 1) should be in the range of 7-8,
56 based on regional intensity reports. Moreover, [Weil-Accardo et al. \(2016\)](#) studied the sea level
57 changes over the last two centuries by analysing morphological changes of microatolls in east-
58 ern offshore Martinique. They underlined the strong possibility of magnitude 7 or more for both
59 historical earthquakes. They also interpreted the long-term subsidence, that was likely due to
60 the 1839 earthquake, as an indicator of the locking of the mantle wedge during the interseismic
61 period.

62 Great population density in Martinique leaves it vulnerable to high risk in case of unpre-
63 paredness for a $M > 7$ earthquake ([Audru et al. 2013](#)). In the absence of a regional seismic
64 hazard study, the assessment of ground motion variability by numerical modelling can guide
65 future mitigation studies. The conventional approach in seismic hazard assessment is the use
66 of ground motion prediction equations (GMPE) that provide estimation of peak ground motion
67 at a distance ([Douglas 2003](#)). A GMPE is developed based on statistical data, and the paucity
68 of large events in LASZ renders a regional GMPE development difficult in Lesser Antilles. In-
69 deed, the only available GMPE, the ‘B3’ model of [Beauducel et al. \(2011\)](#), is limited to events
70 of magnitude less than 6.3. As an alternative to GMPE, numerical modelling offers the possi-
71 bility of better understanding the physical aspect of the phenomenon (i.e., earthquake source
72 and wave propagation). It allows for testing the outcomes of different configurations, which is
73 particularly important for moderately seismic areas such as LASZ.

74 The challenge in numerical modelling is the uncertainty associated with model or input
75 parameters, in particular when working with limited knowledge on earthquake process. The
76 uncertainty related to earthquake source parameters can bring significant variations in the mod-
77 elled ground motion (e.g., [Ripperger et al. 2008](#); [Imperator & Mai 2012](#); [Spudich et al. 2019](#)).
78 This impact is also valid in backward modelling. For example, as shown in [Ragon et al. \(2019\)](#)
79 by their analyses on the 2016 Amatrice, Italy earthquake, accounting for uncertainties of only
80 fault geometry can drastically control the estimated fault slip.

81 Our main objective is to identify the major factors related to earthquake source that can
82 cause ground-motion variability in Martinique during a future M_w 7.5 interplate thrust earth-
83 quake. Within this objective, we prepared 320 rupture scenarios by varying kinematic features
84 of the target hypothetical earthquake. For each scenario, we coupled fault rupture with Empir-
85 ical Green's Functions (EGF) for seismic wave propagation, and predicted broadband ground
86 motion (0.5-25 Hz) at four stations of Martinique. Past studies (e.g., [Ameri et al. 2009](#); [Hartzell](#)
87 [et al. 2002](#); [Pacor et al. 2017](#); [Sørensen et al. 2007](#); [Wang et al. 2009](#); [Withers et al. 2019](#)) under-
88 lined the significant effect of source parameters on ground motion—for example, spatial varia-
89 tions of ground motion amplitudes due to rupture directivity or the location of slip asperities—,
90 and the necessity of accounting for the variability of source parameters to decrease the variabil-
91 ity of the modelled ground motion with respect to GMPEs. Here, we take forward these studies
92 by considering a comprehensive set of source parameters and performing analyses in a broader
93 frequency range.

94 A second objective is to test the role of EGF selection on ground-motion variability. The
95 EGF approach emerges as a powerful method to model broadband ground motion, especially
96 when no detailed knowledge on propagation path is available, as revealed by many applications
97 in the literature (e.g., [Kamae & Irikura 1998](#); [Pulido et al. 2004](#); [Causse et al. 2009](#); [Courboux](#)
98 [et al. 2010](#); [Del Gaudio et al. 2018](#)). It also takes into account possible site effects (except for
99 soil non-linearity) and provides full time histories of ground motion, differently than GMPEs.
100 On the other hand, among the applications in actively seismic areas, EGFs can be selected from
101 foreshocks or aftershocks of a specific earthquake (e.g., [Del Gaudio et al. 2015](#); [Dujardin et al.](#)
102 [2016](#)). Here, we study a moderately-active zone with no successive recordings of such smaller
103 events. In this case, selected events can differ more by several aspects such as seismic moment,
104 stress drop, hypocentre location, etc. As [Pavic et al. \(2000\)](#) denoted, due to such differences be-
105 tween selected EGFs, further variability of ground motion can arise from the EGF method itself.
106 Therefore, we also questioned the influence of EGF selection on ground-motion variability.

107 Scoping these two objectives, the paper is structured as follows: 1) we detail the methods
108 that we used for modelling source kinematics and wave propagation; 2) we explain how we
109 constructed the set of earthquake scenarios and selected moderate earthquakes to employ as

EGF; 3) we address the following three questions, respectively: ‘Which aspect of the source controls the ground motion variability, and why?’; ‘How important is the source-related ground motion variability with respect to the GMPE?’; ‘Is the EGF selection another factor of ground motion variability?’; 4) we discuss the limitations of our study and present the main conclusions.

2 METHODS

We model the target interplate $M_w 7.5$ earthquake by using the kinematic source model of Ruiz’s Integral Kinematics (RIK, Ruiz et al. 2011). RIK model generates, for an earthquake with a prescribed seismic moment, a stochastic slip distribution along with the full slip history—the source-time functions (STF)—at each node of a discretised fault plane. We convolve the output STFs with empirical Green’s functions (EGFs) to compute ground motion at four stations of Martinique. In the following are given the main features of the RIK and EGF methods, respectively.

2.1 Ruiz’s Integral Kinematics (RIK) model

We performed kinematic rupture modelling by using the RIK model implementation of Gallovič (2016). Slight modifications of the original RIK method issued by this implementation are also present here. The numerical tool that we used is an open source code (see Data and resources).

RIK is a composite model that defines an earthquake as a cascade of sub-sources. The number of sub-sources depends on their size, which follows a fractal distribution, i.e. the number of sub-sources with radius greater than a given size is:

$$N = \sum_{i=SUB_{min}}^{SUB_{max}} (2i - 1) \frac{L}{W} \quad (1)$$

where L is fault length; W is fault width; SUB_{min} and SUB_{max} are lower and upper limits of the ratio of fault width to sub-source diameter, respectively.

Each sub-source is a circular fault, or crack—by definition of Eshelby (1957)—that is associated with a slip function of Δu , as follows:

$$\Delta u(r) = \frac{24}{7\pi} \frac{\Delta\sigma}{\mu} \sqrt{R^2 - r^2} \quad (2)$$

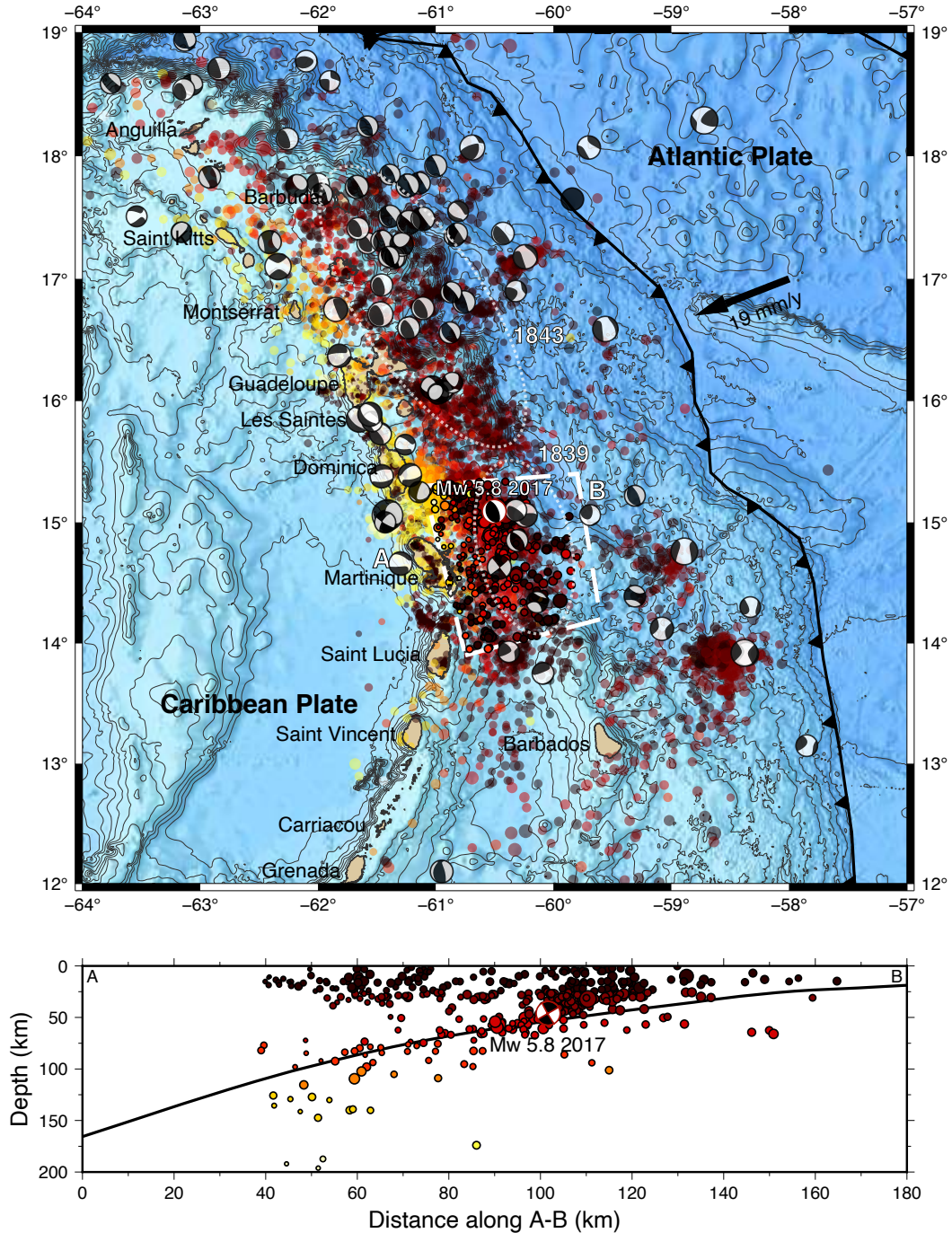


Figure 1. Seismicity of the Lesser Antilles Subduction Zone (LASZ). The dotted ellipses indicate the rupture area of the 1839 and 1843 earthquakes, inferred by [Feuillet et al. \(2011\)](#). The circles, coloured by depth, are the hypocentres from the unified catalogue of the IGP French observatories ([OVSG & OVSM 2020](#)), between 01/01/2014 and 31/12/2019. The dashed white polygon represents the geographical selection made for this study; hypocentres with solid black border within this polygon are recorded by the four broadband stations in Martinique. These hypocentres are also shown on the vertical cross-section, along with the slab model of [Paulatto et al. \(2017\)](#). Focal mechanisms, from GlobalCMT ([Dziewonski et al. 1981](#); [Ekström et al. 2012](#)) are for M5+ earthquakes between 1978 and 2019. Focal mechanism for the 03/02/2017 M_w 5.8 event is from SCARDEC ([Vallée et al. 2011](#)).

128 where $\Delta\sigma$ is the static stress drop; μ is the shear modulus; r is the radial distance to the sub-
 129 source centre; and, R is the sub-source radius. The formula is valid for $r < R$; slip is zero
 130 outside the crack.

RIK model provides a realistic far-field displacement spectrum, with high-frequency ω^{-2}
 decay (ω being the angular frequency). Such a decay is compatible with the observations on
 real earthquakes (Brune 1970), and with dynamic models of circular cracks (e.g., Madariaga
 & Ruiz 2016). In the RIK model, the ω^{-2} decay results from imposing a slip-velocity function
 with a scale-dependent rise time $\tau(R)$ (Ruiz et al. 2011):

$$\tau(R) = \begin{cases} \frac{\alpha L_0}{V_r}, & \text{if } 2R > L_0 \\ \frac{\alpha(2R)}{V_r}, & \text{if } 2R \leq L_0 \end{cases} \quad (3)$$

131 where R is the sub-source radius, α is a constant, that we set to 1 in this study; L_0 is a threshold
 132 of pulse width; and, V_r is the rupture speed. The scale dependency of rise time only applies for
 133 the sub-sources with diameter smaller than L_0 . This feature implies a low-pass filtering effect
 134 on the final slip spectrum.

135 The total slip rate of the modelled earthquake is obtained by summing the slip-rate contri-
 136 bution of each sub-source. More details on the method can be found in Ruiz et al. (2011).

137 2.2 Empirical Green's function (EGF)

138 2.2.1 Formulation

We use the Empirical Green's Function (EGF) method (Hartzell 1978; Irikura 1986) to account
 for seismic wave propagation. This technique starts from the representation theorem (Aki &
 Richards 2002), which expresses the ground displacement $u(x, t)$ at position x and time t :

$$u(x, t) = \int_{\Sigma} s_i(\xi, \tau) * [C_{ijkl}(\xi)v_j(\xi)G_{kl}(x, \xi; t, \tau)] d\Sigma(\xi) \quad (4)$$

139 where \mathbf{s} is the slip vector; \mathbf{C} is the tensor of elastic coefficients; \mathbf{v} is the fault-normal vector; \mathbf{G}
 140 is the Green's function; Σ is the fault surface; and the symbol $*$ denotes time convolution.

In the EGF approach, the second term of the convolution in eq. 4 is replaced by the displacement-
 time history of a real event, $G_{EGF}(x, \xi; \tau)$, located at a position ξ close to the fault and recorded
 at the station position x , after normalising the convolution by the seismic moment of the EGF

event, M_0^{EGF} :

$$u(x, t) = \int_{\Sigma} \frac{\mu}{M_0^{EGF}} S(\xi; \tau) * G_{EGF}(x, \xi; \tau) d\Sigma(\xi) \quad (5)$$

141 In this new formulation, S stands for slip amplitude for a constant rake direction on fault plane
142 and μ is shear modulus.

The integral can be solved by its variational formulation for a discretized fault plane as follows:

$$u(x, t) = \sum_{ij} \frac{\mu^{ij} \cdot l \cdot w \cdot S^{ij}}{M_0^{EGF}} * G^{ij}(x, t) \quad (6)$$

143 where l and w correspond to length and width of the unit area of the discretized fault plane,
144 respectively; M_0^{EGF} is the seismic moment of EGF that is associated with the grid point (ij) .

The discretisation depends on the size of the EGF event. One can construct a fault grid for a target earthquake by using the ratio of the seismic moment between the EGF and target events as a scale factor:

$$n = \frac{L}{l} = \frac{W}{w} = \left(\frac{M_0^{target}}{M_0^{EGF}} \right)^{1/3} \quad (7)$$

145 where L and W are the fault length and fault width of the target event, respectively; l and w are
146 the length and width of unit area of the fault grid, respectively; M_0^{target} is the seismic moment
147 of target event.

148 This approach is based on the assumption of self-similarity of EGF and target events ([Aki](#)
149 [1967](#)), which, in this definition, implies proportionality between slip and rupture length.

150 To satisfy the assumption of similarity between EGF and the target event in eq. 5, the two
151 events should share the characteristics of focal mechanism, location and stress drop. Based on
152 the applications of [Del Gaudio et al. \(2015, 2018\)](#), an earthquake should satisfy the following
153 criteria to be used as EGF: 1) its location should be close enough to that of the target event;
154 2) its focal mechanism should be compatible to that of the target event (difference of faulting
155 angles must be less than 15° and 30° for dip and strike, respectively); 3) its magnitude should
156 allow for a sufficient signal-to-noise ratio; and, at the same time, it should be at least 2 points
157 smaller than the target magnitude.

158 2.2.2 Single-EGF vs Multi-EGF approaches

159 The difference between the single- and multi-EGF approaches lies in the way one associates
 160 the grid points of the fault plane with EGF(s): in the single-EGF approach, all the grid points
 161 use the same EGF for convolution; in the multi-EGF approach, the nearest EGF to grid point is
 162 used. The multi-EGF approach can provide better approximation of observations, as evidenced
 163 by past studies (Del Gaudio et al. 2015; McGuire & Ben-Zion 2017; Del Gaudio et al. 2018). As
 164 mentioned in Introduction, in case of scarcity of successive recordings, the difference of focal
 165 mechanism between the potential EGF events can critically increase such that EGF selection can
 166 become another factor of ground motion variability. Therefore, given the moderate seismicity
 167 of the studied zone, we considered both approaches in our analyses for further comparison.

168 The multi-EGF approach requires a few corrections to bring all the EGFs to an equivalent
 169 energy level and to account for differences between d^{point} (distance between station and grid
 170 point), and d^{hypo} (distance between station and EGF hypocentre). We apply the following steps:

- 171 (i) adjustment of EGF spectra to the same shape (see section 3.3.1);
- 172 (ii) correction of differences in geometrical spreading: each convolution term, for each grid
 173 point, is multiplied by d^{point}/d^{hypo} ;
- (iii) time shift correction: for each grid point, the source time function is shifted by:

$$t_{shift} = \frac{d^{point} - d^{hypo}}{\beta} \quad (8)$$

174 where β is average shear velocity. We use $\beta = 4.5$ km/s, which is the average S-wave value
 175 from Paulatto et al. (2017) tomographic model in the 35-55 km depth range, where the synthetic
 176 faults are placed (see next section).

177 3 EGF SELECTION AND EARTHQUAKE SCENARIOS

178 In this section, we detail the procedure that we followed to select and correct the empirical
 179 Green's functions, and the preparation of earthquake scenarios.

3.1 EGF selection

We extracted from the catalogue of the IPGP Lesser Antilles observatories (see [Data and resources](#)) 423 events, between 01/01/2014 and 02/06/2018, whose epicentral locations are within a polygon offshore Martinique, as shown in Fig. 1. The depth of the selected events range between 0 and 196 km. The events follow the general trends of the subduction zone in terms of depth: they advent as a mix of crustal, interface, and intraplate events (see the discussion in [Introduction](#)). Thus, it is important to closely examine their depth and focal mechanism.

The catalogue only comprises events which have been recorded at each of the four broad-band stations of the ‘West Indies’ network in Martinique (WI, [IPGP 2008c](#); [Anglade et al. 2015](#)): BIM, ILAM, MPOM, and SAM (station locations shown in Fig. 2). We have limited knowledge of site conditions, essentially based on geological maps ([Bureau de recherches géologiques et minières 2018](#)): ILAM and MPOM are on rock, BIM and SAM are on soft soils (SAM is on volcanic ash and pyroclastic flow deposits), and site effects can be present at BIM and ILAM.

Out of the 423 events in our initial catalogue, only three could be selected as EGFs, based on the criteria of distance, magnitude, and focal mechanism discussed in Section 2.2.1. In particular, the desired EGFs: i) are located, in depth, in proximity to the subduction zone, as does the M_w 5.8 earthquake of 03/02/2017 that we use as reference; ii) have a magnitude in the interval of 3.5-5.5; iii) have a focal mechanism of reverse faulting—, and sticking to the flat-thrust characteristic of our target event, we only searched for events in the depth range of 25-65 km. Fig. 2 show the locations of the three events that satisfy these criteria while Table 1 provides details on these EGFs. (Details on the determination of focal mechanism of the catalogued events are provided in SI. Moreover, note that, at the moment of submitting this article, a new solution for EGF II was made available in the catalogue—event `ipgp2017hushqz`, see [Data and resources](#)—, with a slightly different location; we tested the effect of using this new solution on ground motion variability and verified the validity of the conclusions of the present work, as detailed in SI.)

We determined the source properties of the selected three events (moment magnitude, corner frequency and stress drop) by using the SourceSpec software ([Satriano 2020](#)). SourceSpec calculates the earthquake source parameters for an event by inverting the S-wave displacement

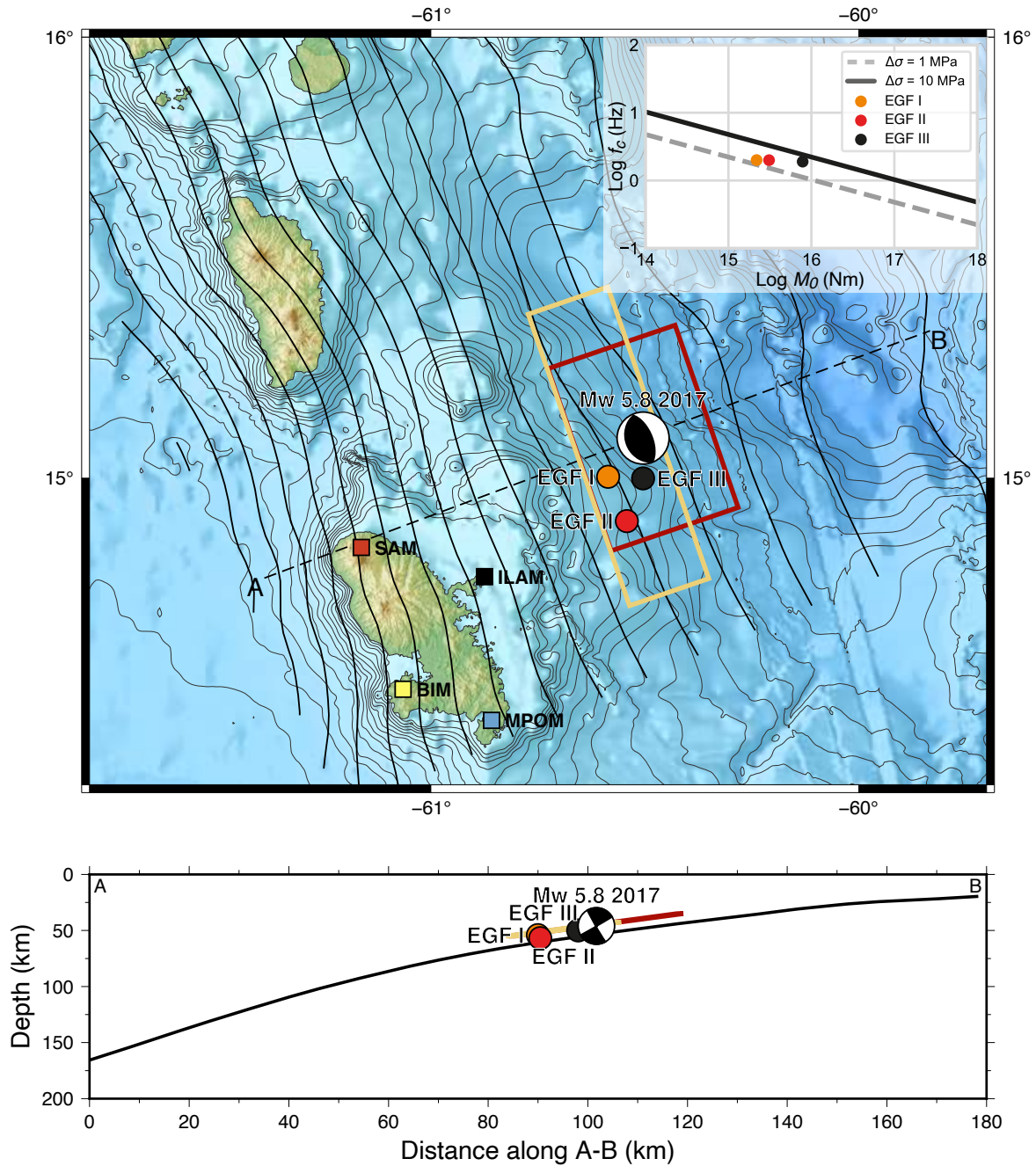


Figure 2. Source and station locations, and source properties of the selected EGFs. Map view of the four selected Martinique stations (WI network), the two fault geometries, the selected EGF events and the focal mechanism of the 2017 $M_w 5.8$ earthquake (top), and vertical section showing the EGFs and the 2017 focal mechanism (bottom). The slab geometry (from Paulatto et al. 2017) is represented by contour lines (10 km depth interval) in top panel and by the solid line in the depth section. Embedded figure displays the corner frequency vs. seismic moment for each selected EGF.

Table 1. Catalogue information (ID, origin time, location, M_L) for the EGFs used in this study and source properties (M_w , f_c , $\Delta\sigma$) obtained from SourceSpec analysis.

EGF	Catalogue ID	Origin Time (UTC)	Long. (° E)	Lat. (° N)	Depth (km)	M_L	M_w	f_c (Hz)	$\Delta\sigma$ (MPa)
I	ipgp2016fkyaql	2016-03-17T18:31:26	-60.56	15.00	54.1	4.12	4.16	2.00	1.99
II	ipgp2017hushqx	2017-04-21T10:13:01	-60.54	14.90	56.8	4.82	4.26	1.99	2.89
III	ipgp2017sep1qy	2017-09-15T10:58:31	-60.50	15.00	50.0	5.04	4.53	1.90	6.16

209 spectra from the recordings of multiple stations. The mean values of source parameters are com-
 210 puted by the average of the results of all the stations. The standard deviation of each parameter
 211 is also calculated; it can increase due to certain factors such as local soil conditions and/or poor
 212 signal quality at station. Therefore, we used all available data (stations from networks CU, G,
 213 GL, MQ, NA, and WI; network information is detailed in [Data and resources](#)) and disregarded
 214 the stations with relatively high deviation to increase the robustness of the solution. Table 1 lists
 215 the results of moment magnitude M_w , corner frequency f_c , stress drop $\Delta\sigma$ for each selected
 216 EGF.

217 In the following, we will only consider moment magnitudes. Fig. 2 shows the relation be-
 218 tween corner frequency and seismic moment of each event with respect to stress drop. The stress
 219 drop of each EGF is between 1 and 10 MPa. The stress drop of EGF III is notably higher than
 220 that of the other two events.

221 3.2 Earthquake scenarios

222 We prepared a set of earthquake scenarios for an interplate M_w 7.5 earthquake, comprising
 223 of 320 different kinematic rupture models. To take into account different aspects of source
 224 kinematics, we constructed a logic tree where each branch explores a different source parameter
 225 (Fig. 3). In the following, we briefly explain these aspects by hierarchical order.

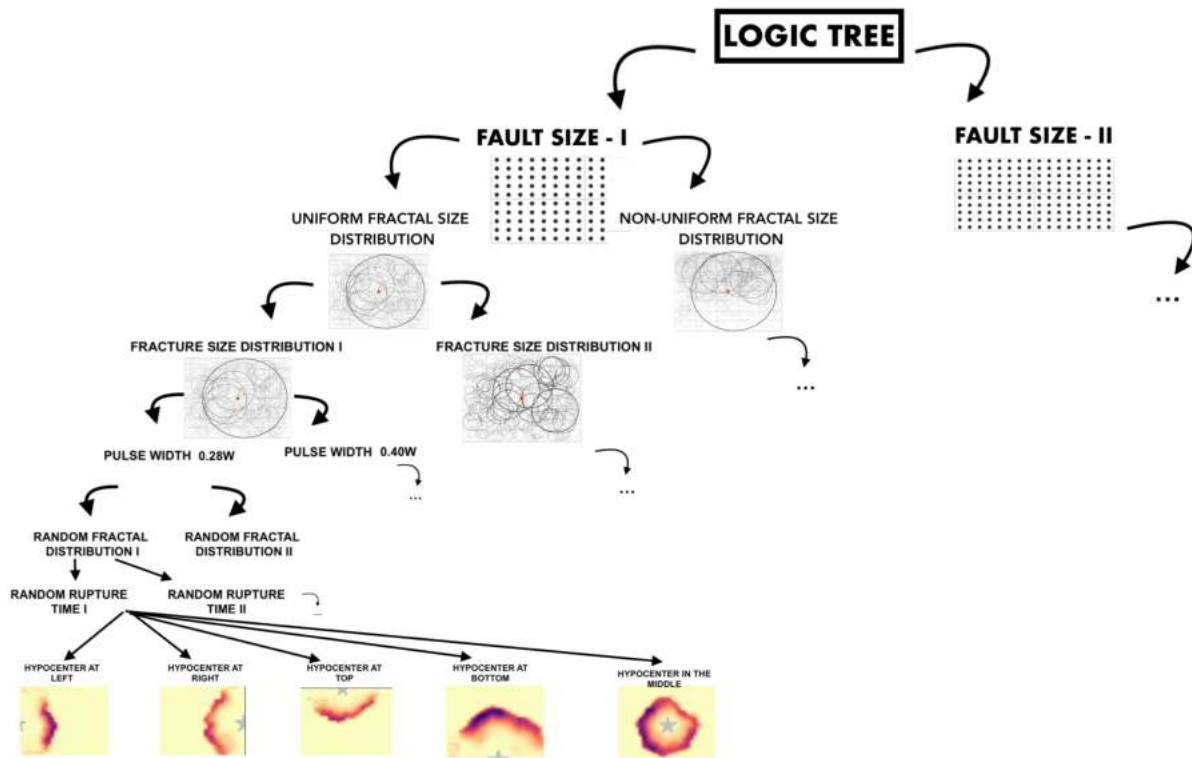


Figure 3. Illustration of the logic tree organisation for generating earthquake scenarios. Three dots indicate the repetition of sub-branches similar to those of neighbour branch.

226 3.2.1 Fault geometry

227 The logic tree starts with the main branches of fault geometry. We created two models: 1) a
 228 fault with a low aspect ratio (square-like) with dimensions of $50 \text{ km} \times 40 \text{ km}$; 2) a fault with a
 229 high-aspect ratio (rectangular) with dimensions of $80 \text{ km} \times 25 \text{ km}$.

230 We fixed the fault location and orientation based on a reference event, the 03/02/2017
 231 M_w 5.8 earthquake (Fig. 2). The focal mechanism of this event was reported as reverse faulting
 232 with strike, dip and rake angles of 161° , 30° and 94° , respectively, and hypocentre is located
 233 at 46 km depth (SCARDEC data by Vallée et al. 2011). We set our maximum fault depth to
 234 55 km in all cases, by respecting the past documentation on seismogenic zone (e.g., Paulatto
 235 et al. 2017). We defined the midpoint of the first type of fault geometry at the hypocentre co-
 236 ordinates of the 03/02/2017 event (15.090° N , 60.504° W). In this way, the fault plane extends
 237 between 35-55 km and 42.5-55 km depths for the first and second types of geometries, respec-
 238 tively. Fig. 2 depicts the location of two fault geometries in map view and cross section. The

239 alignment of fault planes are slightly shallower with respect to the slab, but in good agreement
240 with the depth of recorded events.

241 3.2.2 *Spatial distribution of sub-sources*

We created two sub-branches to test the effect of using uniform or dip-varying spatial distribution of large sub-sources. In uniform-distribution model, we evenly distributed the sub-sources all over the fault plane; in dip-varying distribution model, we define the along-dip probability to have a sub-source as:

$$P(d) = \cos^9 \left(\frac{\pi d}{2W} \right),$$

where d is the along-dip distance and W is fault width: $P(0) = 1$ at fault top; $P(W) = 0$ at fault bottom. The power of nine was arbitrarily chosen to increase the relative probability close to the fault top with respect to the fault bottom. From this probability function, we define a sub-source size-dependent probability

$$\bar{P}(R, d) = P(d)^{\gamma(R)}$$

$$\gamma(R) = \frac{R - R_{min}}{R_{max} - R_{min}}.$$

242 Hence, for the largest sub-source, the probability density function equals $P(d)$; and for the
243 smallest one it equals 1, i.e., being uniform over the fault plane.

244 3.2.3 *Sub-source size*

245 We tested the effect of the presence of the largest sub-source, with diameter equal to fault
246 width. The first sub-branch allows for a relatively large range of sub-source sizes: the largest
247 and smallest radii equal 100 % and 5 % of fault width, respectively. We lowered the largest
248 radius to 50 % in the second group.

249 3.2.4 *Pulse width, L_0*

250 As mentioned in Section 2.1, this parameter produces a low-pass filtering effect on slip spec-
251 trum, and hence can influence the ground motion amplitude. We tested the power of such in-

fluence by adding two sub-branches: 1) $L_0 = 0.28$; 2) $L_0 = 0.4$. More explanation on why we
 have chosen these values is provided in Supplementary Information (SI).

3.2.5 Random parameters, $idum1$ and $idum2$

The numerical tool that we use incorporates two parameters, $idum1$ and $idum2$, that control the
 randomness of the spatial distribution of sub-sources and propagation of rupture front on fault
 grid, respectively. We created two additional orders of sub-branches to account for each of this
 randomness.

3.2.6 Rupture directivity

We created a last order of sub-branches to test the effect of rupture directivity, by varying the
 hypocentre location. We prepared five cases based on the relative location of hypocentre on fault
 plane: left, right, top, bottom, centre.

3.3 EGF correction and coupling with kinematic rupture model

3.3.1 EGF correction

We adjusted all selected EGFs to the same spectral shape that corresponds to a reference spec-
 trum for a M_w 4.2 event. The philosophy of EGF correction is to reduce significant variation of
 ground motion amplitudes that can possibly arise from the difference of stress drop of selected
 EGFs (Hutchings et al. 2007; Del Gaudio et al. 2015). For the reference spectrum, we set the
 stress drop, corner frequency, and seismic moment to the mean of EGFs' values: 1.917 MPa,
 2.027 Hz, and 2.5119×10^{15} Nm, respectively. For each station record of each EGF, the adjust-
 ment procedure applies as follows:

- (i) computation of the Fourier transform of displacement;
- (ii) conversion of displacement spectrum in seismic moment unit;
- (iii) deconvolution (amplitude division) of the converted spectrum by Brune's spectrum that
 corresponds to the corner frequency and seismic moment of the uncorrected EGF—this step is
 similar to the application in Dujardin et al. (2016);
- (iv) multiplication of the deconvolved spectrum with the mean seismic moment.

EGF III corrected for the NS component of station BIM

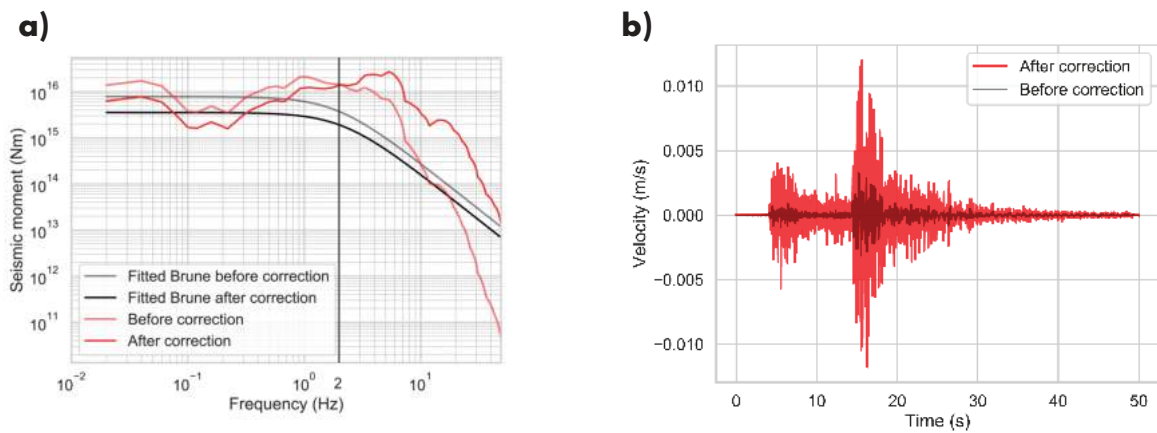


Figure 4. Example of EGF correction. a) Moment spectra of the north-south component of EGF III signal at station BIM before and after correction. b) Velocity-time histories before and after correction.

278 Operations of steps (iii) and (iv) would provide a flat spectrum beyond the corner frequency
 279 when inelastic attenuation is ignored. Here however we preserve the attenuation information
 280 on the final spectrum by not including anelastic (and geometric) attenuation in the Brune's
 281 spectrum which is deconvolved in step (iii). Final step of signal processing includes: removal of
 282 instrumental response, detrending, and band-pass filtering in the frequency band of 0.01-49 Hz.

283 Fig. 4a shows an example of spectral adjustment of EGF III for the north-south component
 284 of station BIM. All the spectra are smoothed with a Hanning window of the 5th degree. We
 285 see in the example that the spectrum is deamplified after correction at frequencies below the
 286 corner frequency of reference spectrum (~ 2 Hz) since the seismic moment of the uncorrected
 287 EGF is higher than the reference one. The flattening effect of EGF adjustment beyond corner
 288 frequency produces an amplification at frequencies above ~ 2 Hz; however, due to the pre-
 289 served inelastic attenuation, the resultant spectrum still shows a decay for frequencies above
 290 ~ 7 Hz. The resulting signal in time domain depicts notable amplification—up to 4 times for
 291 peak values—throughout the signal duration due to correction, as shown in Fig. 4b.

292 3.3.2 Coupling with kinematic rupture model

293 We discretized the fault plane based on the ratio of seismic moment between the target and
 294 EGF events, that equals 4. Referring to eq. 7, our fault grid contains 1600 points for all rupture
 295 models.

296 For each grid point, the corresponding source time function is convolved with the nearest
297 EGF in 3D space. One example of such partition for the case of a fault with low-aspect ratio (the
298 1st type of fault geometry in the logic tree) is given in SI (Fig. S1). We then made additional
299 corrections as detailed in Section 2.2.2. The modelled ground motion at a station issued by the
300 target earthquake equals the sum of the corrected convolutions. The velocity and density profile
301 that we used is provided in SI.

302 The frequency band which we considered for ground motion modelling is 0.5-25 Hz, based
303 on signal quality. We further analysed the signal-to-noise-ratio (SNR) of each EGF recordings
304 for each station. Except for the cases with slightly lower SNR values, all the cases provide SNR
305 values above 5 in the frequency band of 0.5-25 Hz. Therefore, we will refer to this frequency
306 band in the evaluation of our ground motion models.

307 **4 RESULTS**

308 We evaluate the results for the 320 simulated scenarios, through the following parameters: peak-
309 ground acceleration (PGA), spectral acceleration (SA) values at 1, 2 and 5 Hz, and Arias inten-
310 sity. We made these analyses on the maximum of the three components. [Lancieri et al. \(2015\)](#)
311 showed that these are the most influential parameters on seismic structural analysis.

312 **4.1 Fault geometry and sub-source size cause the highest variability of ground motion**

313 The first question we wanted to address is: ‘Which aspect of the source controls ground motion
314 variability?’. To answer this question, we evaluated the model outputs by considering each
315 branch of the logic tree (Fig. 3). To account for both amplitude and energetic content of the
316 calculated ground motion, we disaggregated the simulation results based on PGA and peak
317 Arias intensity. Fig. 5 shows disaggregation for station ILAM (the analyses on the other stations
318 lead to the same conclusion, as shown in SI). Our analyses on all four stations highlight a
319 distinctive clustering due to the fault geometry and sub-source size: a low aspect ratio of fault
320 geometry brings relatively low energetic ground motion (cluster A); whereas, a high aspect
321 ratio of fault geometry together with smaller slip asperities—i.e., a rectangular fault where sub-

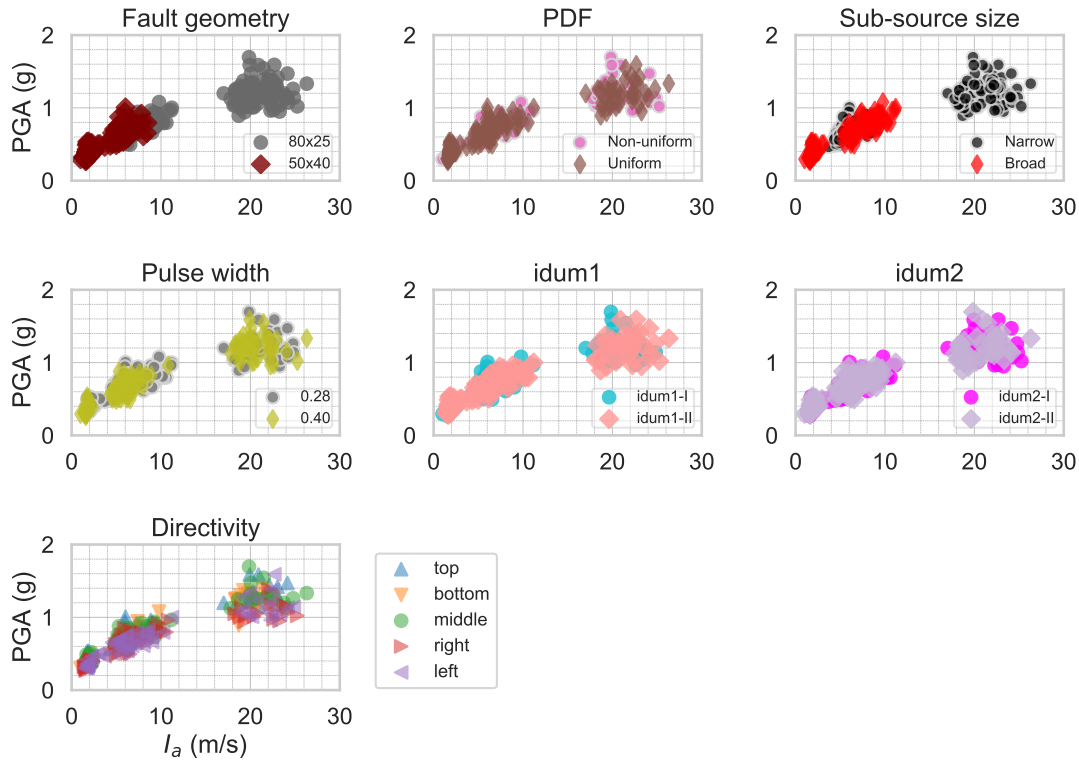


Figure 5. Disaggregation of computed ground motion by PGA and peak Arias intensity for station ILAM. We classified the results by different parameters in each diagram: by fault geometry, spatial distribution of sub-sources (PDF), sub-source size, pulse width, idum1, idum2, and directivity. The choice of fault geometry and sub-source size parameters are the causative factors of two distinct clusters, which we call ‘A’ and ‘B’.

322 sources larger than 50% of fault width are forbidden—results in a notable amplification of peak
 323 ground motion (cluster B).

324 Such clustering implies a significant change of wave energy throughout the signal duration
 325 and in a broad frequency range (0.5-25 Hz). We picked a representative case from each of
 326 the above-mentioned two clusters A and B. We compared the two cases by acceleration-time
 327 histories, their Fourier amplitudes, and temporal change of Arias intensities. Fig. 6 displays
 328 this comparison for all stations. The cluster B case evicts a higher level of wave energy at all
 329 stations: PGA is approximately 2.5 times higher, and the peak Arias intensity can reach to 10
 330 times higher values for all stations.

331 We found that the combination of a fault geometry with a high aspect ratio and a spatially-
 332 condensed largest slip distribution, i.e., smaller patches with greater slip values, makes a double
 333 effect of amplification of source energy; and, this double energy boost leads to the clustering of

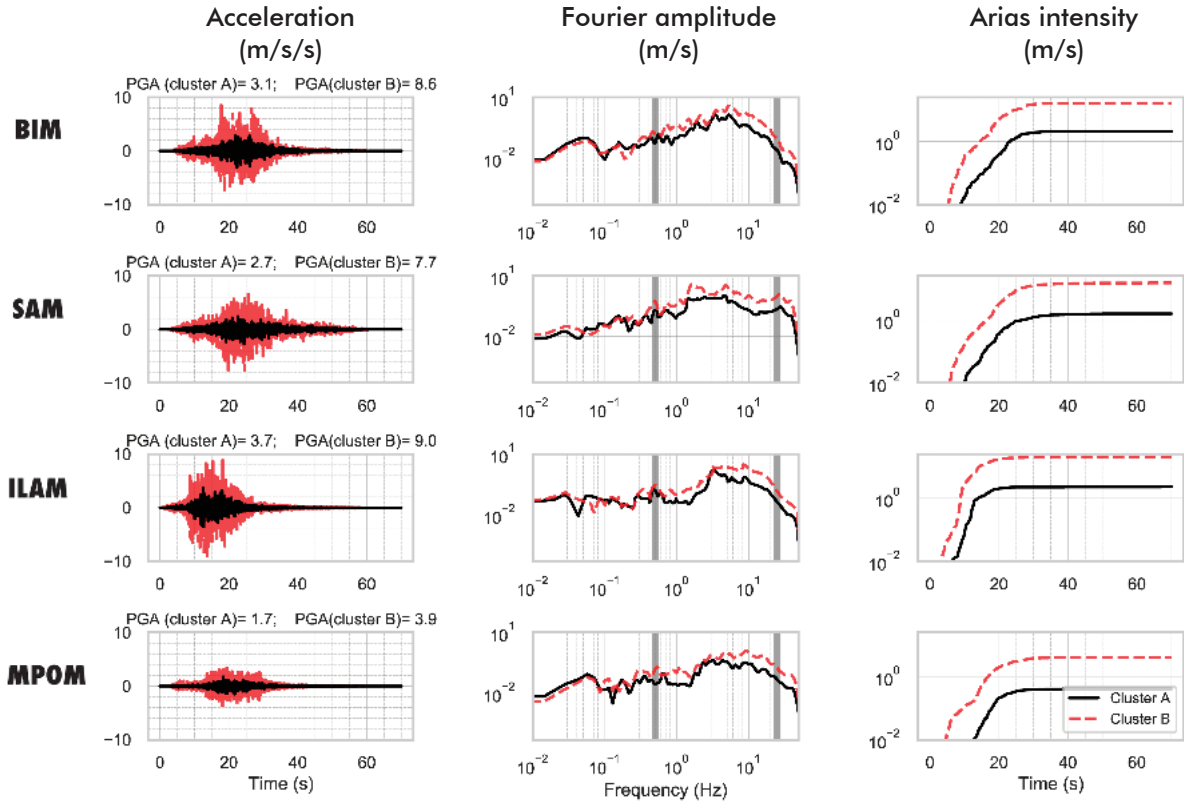


Figure 6. Comparison of acceleration-time histories (left panel), Fourier amplitude (middle panel), and Arias intensities (right panel) between cluster A (in black) and cluster B (in red) (see Fig. 5). We used the north-south component of signals in each comparison. Each row corresponds to the results of a station: BIM, SAM, ILAM, and MPOM, from top to bottom, respectively. The frequency band of 0.5-25 Hz is indicated by grey bars.

334 ground motion. We compared the two clusters by sub-source distribution (a), final slip distri-
 335 bution (b), and STF (moment-rate time function) and moment spectra (c) (Fig. 7). Our analysis
 336 evidences that:

337 (i) The presence of the sub-source with a diameter equal to fault width (cluster A) results in a
 338 spatially extensive slip asperity such that a significant part of the fault plane undergoes relatively
 339 large slip. Yet, the lack of such big-size sub-source (cluster B) results in a slip distribution where
 340 the largest values are spatially concentrated in relatively small patches. This leads to a partial
 341 amplification of source energy in the whole frequency band, in particular above 1 Hz.

342 (ii) The fault geometry with high aspect ratio (cluster B) can result in a rupture propaga-
 343 tion that is longer and in a composite source-time function with multiple peaks and shorter rise
 344 time—individual slip-rate functions become spiky (short rise time) in the cluster B case, differ-

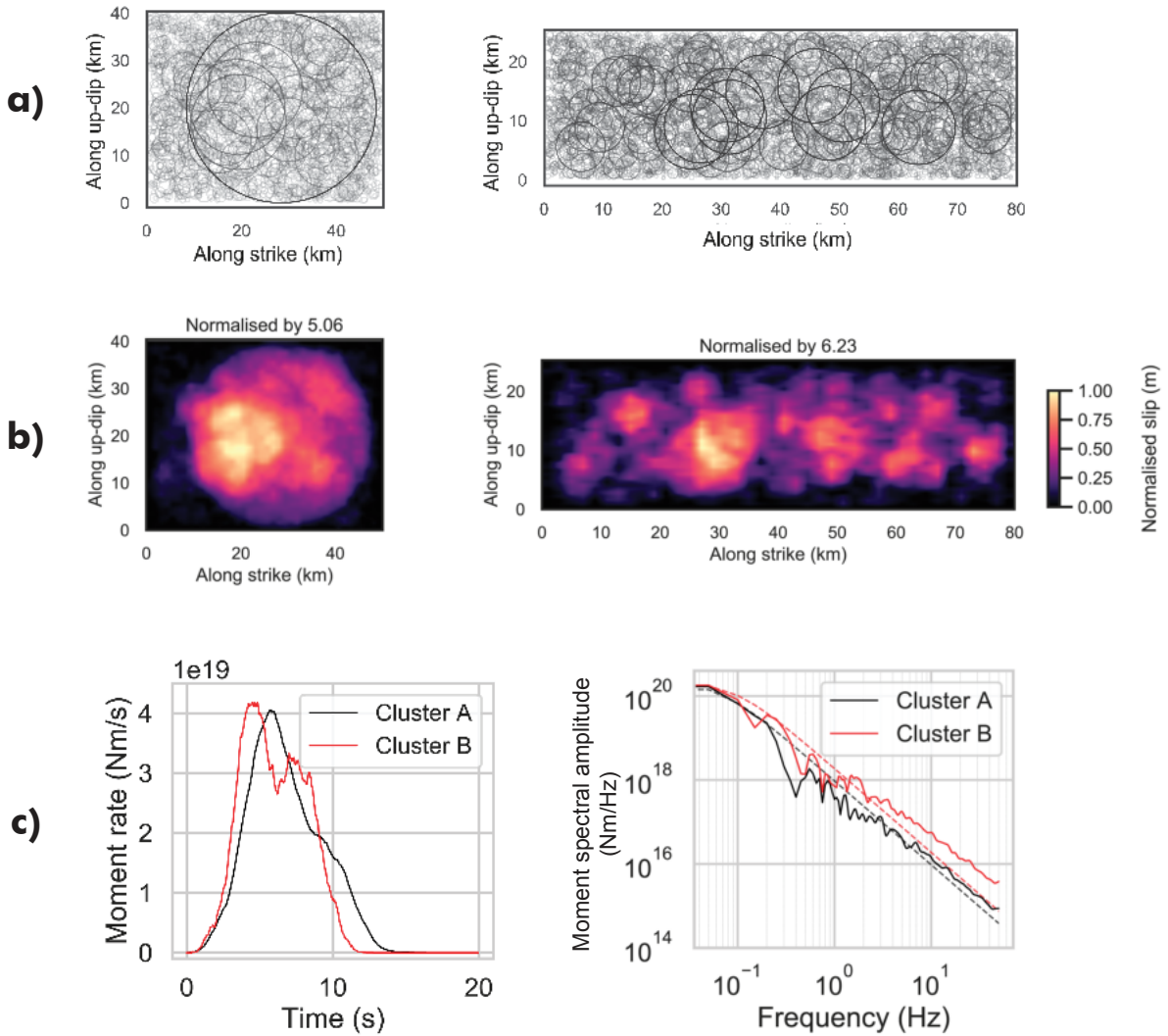


Figure 7. Comparison of source features of the two clusters shown in Fig. 5. a) Comparison of cluster A (left panel) and cluster B cases (right panel) by sub-source distribution. b) Same as a) for final slip distribution. c) Comparison of source-time function (left panel) and moment spectra (right panel) between cluster A (in black) and cluster B (in red) cases.

345 ently than the case of cluster A that has smooth STFs (see details in SI). This complexity also
 346 partially contributes to the energy amplification in the whole frequency band.

347 **4.2 Comparison with GMPE: source-related variability influences the compatibility of** 348 **estimated ground motion with GMPE**

349 The second question we wanted to address is: ‘How important is the source-related ground
 350 motion variability with respect to the GMPE?’. In previous section, we evidenced two clusters

351 of synthetic ground motion due to the differences of source definition. Here, we evaluate this
352 ground-motion variability by referring to the compatibility of modelled data with GMPE.

353 [Bozzoni et al. \(2011\)](#) compiled all the available databases in Eastern Caribbean Islands and
354 analysed different GMPEs that have been developed for other regions with similar seismotec-
355 tonic settings. They recommend the GMPE of [Zhao et al. \(2006\)](#) for the type of events we study
356 here, namely plate interface earthquakes with a reverse faulting mechanism. A similar conclu-
357 sion was made in a later study by [Douglas & Mohais \(2009\)](#). The GMPE of [Zhao et al. \(2006\)](#)
358 consists of four soil categories: rock, hard soil, medium soil, and soft soil. In the absence of a
359 detailed knowledge on site conditions, we have chosen the site condition of soft soil. We ver-
360 ified by using other site conditions that this choice only causes slight variations of amplitude
361 and does not change our conclusions (see figures in SI).

362 The two clusters of synthetic ground motion have two different levels of ground motion
363 amplitude by distance. The compatibility of these trends with GMPE, for M_w 7.5 strongly
364 depends on frequency and station. Fig. 8 shows the comparison of synthetic ground motion and
365 GMPE curves for spectral acceleration (SA) analyses at 1, 2, and 5 Hz. We make the comparison
366 separately for each station, and the hypocentral distance at each simulation varies based on the
367 definition of hypocentre. In general, cluster B is associated with higher amplitude of ground
368 motion at all distances. At 1 Hz, the majority of the synthetic ground motion agrees well with
369 GMPE for stations BIM and SAM; but, the ground motion at the same frequency is mostly
370 underestimated for stations ILAM and MPOM. At 2 Hz, SAs for cluster A align with mean
371 GMPE predictions for the stations BIM and SAM, whereas they are closer to lower limit of
372 GMPE predictions for the other two stations. At 5 Hz, the cluster B entirely overestimates the
373 GMPE predictions for all stations except for MPOM, and the agreement of the first cluster with
374 GMPE still remains station-dependent. The comparative analysis of PGA prediction between
375 the synthetic data and GMPEs gives the same conclusion as we show here for SA at 5 Hz: the
376 synthetic data in cluster B overestimates the GMPE predictions for all stations, and the cluster
377 A data mostly fall into the predicted range of GMPEs for only MPOM (details provided in SI).

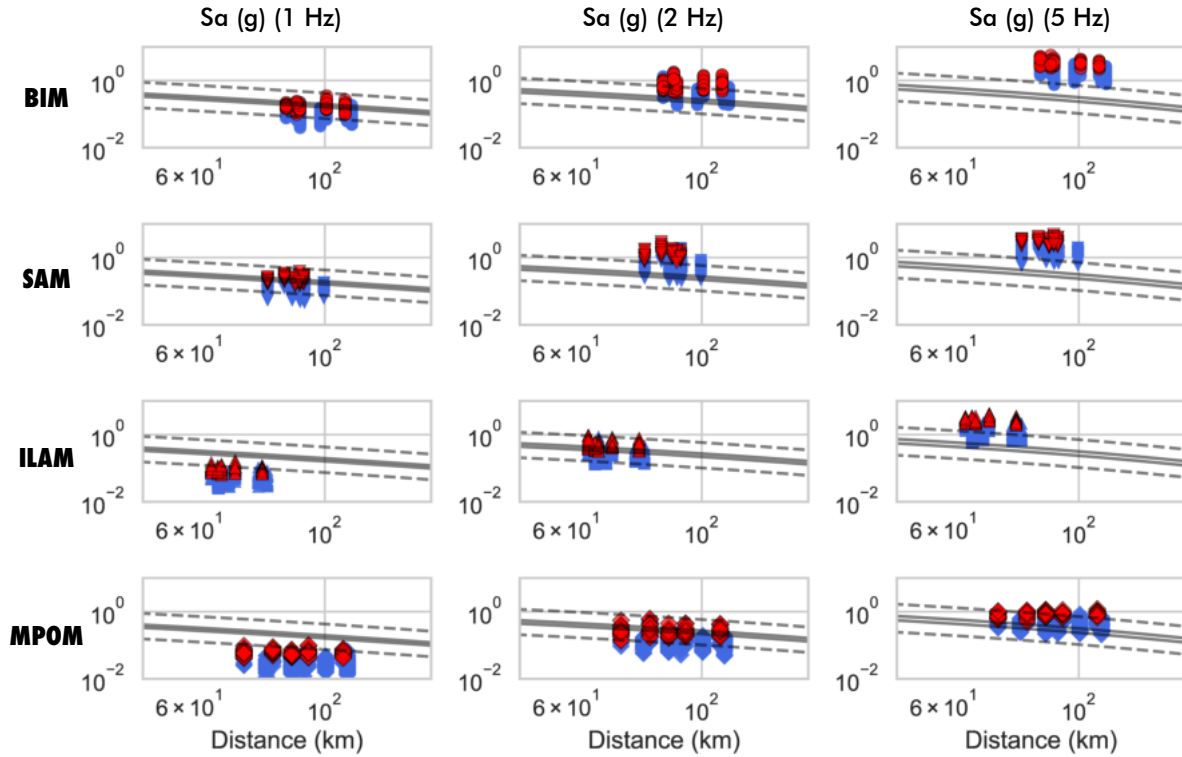


Figure 8. Comparison of cluster A (in blue) and cluster B (in red) cases of synthetic ground motion with GMPE curves from [Zhao et al. \(2006\)](#) (in gray) by spectral acceleration at 1 Hz (left panel), 2 Hz (mid-panel), and 5 Hz (right panel). Mean GMPE curves are shown in solid lines; the lower and upper limits of GMPE curves are shown in dashed lines. Each row stands for the analysis of a station: BIM, SAM, ILAM, and MPOM from top to bottom, respectively.

4.3 EGF selection can emerge as a station-dependent factor of ground-motion variability

The third question we aimed to address is: ‘Does EGF selection further influence ground motion estimations?’ The analyses in previous sections were based on the multi-EGF approach in order to focus exclusively on the effects of source-related factors on ground motion variability. Here we explore the role of the EGF selection by repeating the logic tree simulations for each single-EGF use.

We found that the predicted ground motion can be highly sensitive to EGF selection: the energy difference of EGFs in a specific frequency band can become a factor of ground-motion variability despite the EGF corrections. We categorised the synthetic data by EGF use as shown

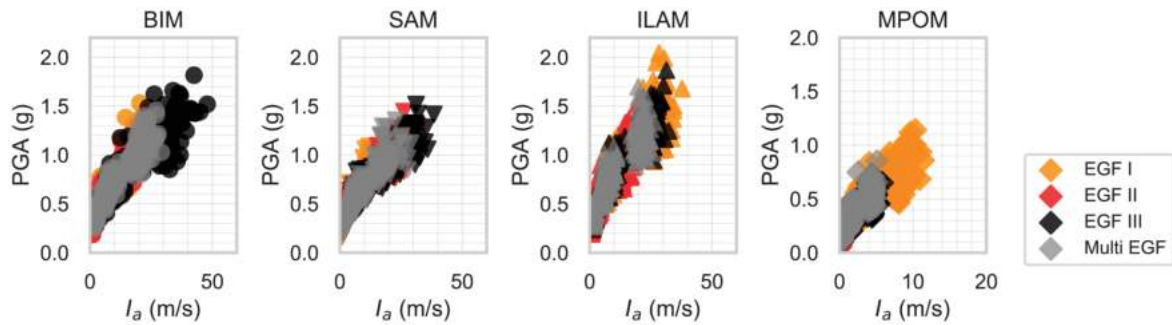


Figure 9. Effect of EGF selection on ground motion. Comparison of peak ground acceleration vs peak Arias intensity results between all EGF approaches. Each diagram shows the results for a station.

in Fig. 9. Stations BIM and MPOM exhibit notably higher ground motion amplitudes for the use of EGF III and EGF I, respectively.

5 DISCUSSION

5.1 Variation of ground motion between stations

The range of ground motion amplitude strongly varies between the four stations; In general, we computed a weaker ground motion amplitude for station MPOM compared to other stations. Fig. 10 shows histograms and kernel density estimations (KDE) of computed PGA for all performed simulations. KDE is a way of visualising the shape of the sample distribution (Parzen 1962; Davis et al. 2011); it is defined as the normalised sum of kernel functions of a certain width computed on the data samples (here we use Gaussian kernels of standard deviation 0.27, 0.26, 0.32, and 0.15 g for stations BIM, SAM, ILAM, and MPOM, respectively; details on KDE can be found in the reference provided in Data and resources). The results point to a similarity between three stations, BIM, SAM and ILAM, in terms of amplitude and standard deviation: Average PGA of the cluster A ranges between 0.57 and 0.75 g for the three stations. On the other hand, this value lowers to 0.31 g for station MPOM. The peak kernel density notably increases, approximately twice, at station MPOM due to the narrow range of PGA, i.e., limited variation, compared to the other stations.

A detailed site characterisation is essential to better assess the variation potential of ground motion between the stations and understand the reason behind it. Recall that we found that the

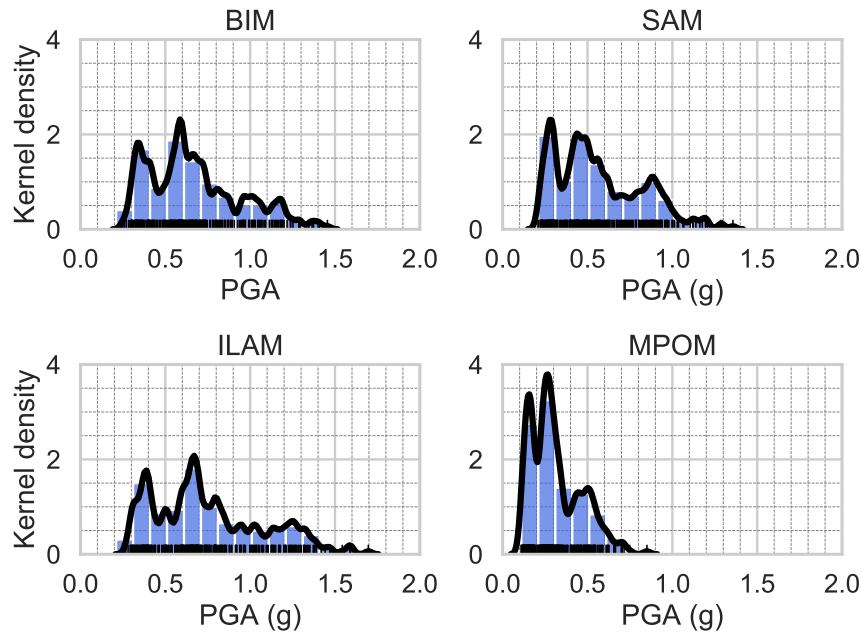


Figure 10. Histograms of peak ground acceleration values at each station, associated with kernel density (black curve). Each rug stands for a simulation result.

407 significance of ground motion variability with respect to GMPE and the potential of further
 408 variability due to EGF selection are station-dependent. Our current knowledge about site condi-
 409 tions is limited and does not allow for further interpretations of the variation of ground motion
 410 between stations in our results. Additional analyses to characterise site effects at Martinique
 411 stations—as applied in Guadeloupe ([Castro et al. 2003](#))—would be helpful for future seismic
 412 hazard studies in Martinique. Moreover, EGF method considers a similarity of the source-to-site
 413 propagation path between EGF and target earthquake; it cannot account for further variation of
 414 ground motion due to possible site-related complexities due to a strong earthquake. We target
 415 a magnitude 7.5 earthquake, and further variation of ground motion due to complex soil be-
 416 haviour (e.g., soil nonlinearity, and liquefaction) under such a strong earthquake is possible as
 417 known by past observations and numerical studies (e.g., [Aguirre & Irikura 1997](#); [Ghofrani et al.](#)
 418 [2013](#); [Régnier et al. 2013](#); [Oral et al. 2019](#)). Further research on this aspect, together with an
 419 enhanced site characterisation, can take the variability analysis a step forward.

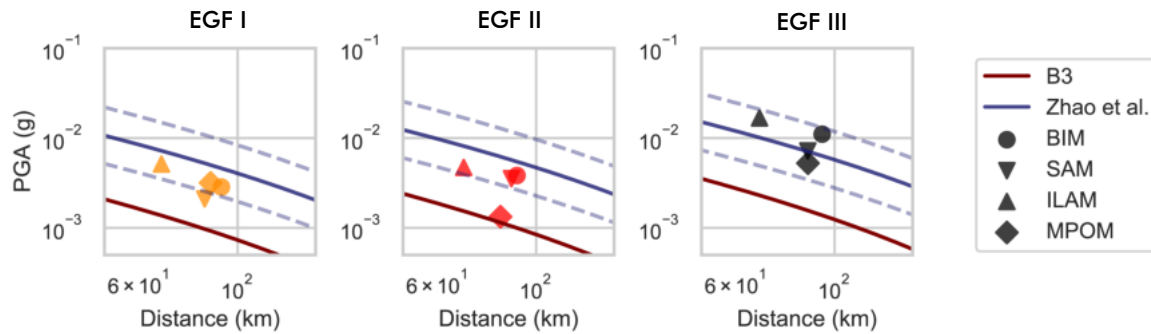


Figure 11. Comparison of PGA prediction curves of [Zhao et al. \(2006\)](#) model (in gray) and B3 model (in red) with observations at four stations: BIM, SAM, ILAM, and MPOM. Results are shown for the three selected EGF events: EGF I (left panel), EGF II (mid-panel), and EGF III (right panel).

420 5.2 Need for an improved regional GMPE

421 The absence of a regional GMPE for a magnitude 7.5 earthquake is another limitation for the
 422 interpretation of our results; the only regional GMPE, the ‘B3’ model ([Beauducel et al. 2011](#)),
 423 also needs revision for moderate events. Here we used the GMPE of [Zhao et al. \(2006\)](#), that was
 424 developed with Japanese data, to analyse our synthetic ground motion data, since the B3 model
 425 is not recommended for $M \geq 6.5$ earthquakes. Although past studies qualify the [Zhao et al.](#)
 426 (2006) GMPE as the best representative of our target earthquake, [Kotha \(2018\)](#) states that the
 427 use of a GMPE that has been developed with the data from a different region can become non-
 428 ergodic due to the differences of crustal characteristics. Therefore, according to the latter, such
 429 GMPEs require additional adjustments of ground motion before application to other regions. In
 430 that sense, future mitigation studies would benefit from further research on GMPE applications.

431 We compared the B3 model and [Zhao et al. \(2006\)](#) GMPE with the EGF recordings, in a
 432 range of magnitudes (4.2–4.5) where both GMPEs are valid (Fig. 11). B3 model underestimates
 433 all the three events, whereas [Zhao et al. \(2006\)](#) is mostly in agreement with observations. This
 434 incompatibility also points to further need to improve regional GMPE applications.

435 **6 CONCLUSIONS**

436 A future $M > 7$ interplate earthquake is expected offshore Martinique. In this study, we in-
437 vestigated the potential sources of broadband ground motion variability mainly due to source
438 kinematics for a hypothetical M_w 7.5 earthquake.

439 Our findings are:

440 (i) The fault geometry and the spatial extension of the largest slip patch are the most determi-
441 nant source-related factors of ground motion variability. The combination of a rectangular fault
442 with a high aspect ratio and condensed small slip asperities can result in a significant amplifi-
443 cation of source energy. Such energy amplification manifests itself by a substantial increase of
444 broadband wave energy and ground motion amplitude throughout the signal duration. We stress
445 that we set the down-dip limit to 55 km, as suggested by [Paulatto et al. \(2017\)](#) for the coupled
446 interface of the subduction zone; more studies are needed to constrain the further role of the
447 fault geometry when considering different depths of the down-dip limit.

448 (ii) The significance of the source-related ground motion variability with respect to GMPE
449 depends on the evaluated frequency of ground motion and station. Future research on the im-
450 provement of regional GMPE application and site characterisation is necessary to constrain the
451 realistic range of ground motion and source parameters.

452 (iii) EGF selection can be another factor of ground-motion variability. The application of
453 EGF technique for forward modelling in moderately seismic areas such as Martinique requires a
454 special attention to EGF selection, because of potential energy differences between EGF events.

455 **ACKNOWLEDGEMENTS**

456 This study is funded by the convention between Institut de Physique du Globe de Paris and
457 General Directorate of Prevention of Risks of French Ministry for the Ecological and Inclusive
458 Transition and by the project "Vers la Plateforme Régionale de Surveillance Tellurique du futur"
459 (PREST) co-funded by INTERREG Caraïbes for the European Regional Development Fund.

460 We would like thank to Sergio Del Gaudio, František Gallovič, and Jean-Marie Saurel for
461 their substantial help in applying the method of multi-EGF, using the RIK model, and in re-

462 retrieval of the seismic catalogue of the Lesser Antilles, respectively. We also acknowledge the
463 fruitful discussions with Pascal Bernard, Luis Fabian Bonilla, Pierre-Yves Bard, and Jean-Paul
464 Ampuero, that definitely improved the quality of this work.

465 **Data and resources**

466 The seismic catalogue for Lesser Antilles used in this study is available from [OVSG & OVSM](#)
467 ([2020](#)). Note that event `ipgp2017hushqx` is not present in the catalogue, since it has been
468 superseded by event `ipgp2017hushqz` (see discussion in [EGF selection](#)).

469 Waveform data from networks G, WI, GL and MQ ([IPGP & EOST 1982](#); [IPGP 2008c,a,b](#))
470 was downloaded from the IPGP Data Center (<http://datacenter.ipgp.fr>).

471 Waveform data from networks CU and NA ([Albuquerque Seismological Laboratory \(ASL\)/USGS](#)
472 [2006](#); [KNMI 2006](#)) was obtained through the IRIS Data Management Center (<https://ds.iris.edu/ds/nodes/dmc/>).

473
474 The RIKsrf code, used for modelling kinematic source rupture, is available at <https://github.com/fgallovic/RIKsrf>. The SourceSpec code, used to determine earthquake source
475 parameters, is available at <https://github.com/SeismicSource/sourcespec>.

476
477 Data analysis has been performed using ObsPy ([Krischer et al. 2015](#)). Figures have been
478 produced using the Generic Mapping Tools ([Wessel et al. 2019](#)) and Matplotlib ([Hunter 2007](#)).

479 Explanation of seaborn library tools of Python to visualise kernel density plots can be
480 found at <https://seaborn.pydata.org/tutorial/distributions.html> and <https://mathisonian.github.io/kde/>.

482 **REFERENCES**

- 483 Aguirre, J. & Irikura, K., 1997. Nonlinearity, liquefaction, and velocity variation of soft soil layers in
484 Port Island, Kobe, during the Hyogo-ken Nanbu earthquake, *Bulletin of the Seismological society of*
485 *America*, **87**(5), 1244–1258.
- 486 Aki, K., 1967. Scaling law of seismic spectrum, *Journal of Geophysical Research*, **72**(4), 1217–1231,
487 doi: [10.1029/JZ072i004p01217](https://doi.org/10.1029/JZ072i004p01217).
- 488 Aki, K. & Richards, P., 2002. *Quantitative Seismology*, University Science Books.

- 489 Albuquerque Seismological Laboratory (ASL)/USGS, 2006. Caribbean usgs network, doi:
490 [10.7914/SN/CU](https://doi.org/10.7914/SN/CU).
- 491 Ameri, G., Gallovič, F., Pacor, F., & Emolo, A., 2009. Uncertainties in strong ground-motion prediction
492 with finite-fault synthetic seismograms: An application to the 1984 M 5.7 Gubbio, central Italy, earth-
493 quake, *Bulletin of the Seismological Society of America*, **99**(2A), 647–663, doi: [10.1785/0120080240](https://doi.org/10.1785/0120080240).
- 494 Anglade, A., Lemarchand, A., Saurel, J.-M., Clouard, V., Bouin, M.-P., Chabalier, J.-B. D., Tait, S.,
495 Brunet, C., Nercessian, A., Beauducel, F., Robertson, R., Lynch, L., Higgins, M., & Latchman, J.,
496 2015. Significant technical advances in broadband seismic stations in the Lesser Antilles, *Advances*
497 *in Geosciences*, **40**, 43–50, doi: [10.5194/adgeo-40-43-2015](https://doi.org/10.5194/adgeo-40-43-2015).
- 498 Audru, J. C., Vernier, J. L., Capdeville, B., Salindre, J. J., & Mouly, E., 2013. Preparedness actions
499 towards seismic risk mitigation for the general public in Martinique, French Lesser Antilles: a mid-
500 term appraisal, *Natural Hazards and Earth System Sciences*, **13**(8), 2031–2039, doi: [10.5194/nhess-](https://doi.org/10.5194/nhess-13-2031-2013)
501 [13-2031-2013](https://doi.org/13-2031-2013).
- 502 Beauducel, F., Bazin, S., Bengoubou-Valerius, M., Bouin, M.-P., Bosson, A., Anténor-Habazac, C.,
503 Clouard, V., & De Chabalier, J.-B., 2011. Empirical model for rapid macroseismic intensities pre-
504 diction in Guadeloupe and Martinique, *Comptes Rendus Géoscience*, **343**(11-12), 717–728, doi:
505 [10.1016/j.crte.2011.09.004](https://doi.org/10.1016/j.crte.2011.09.004).
- 506 Bozzoni, F., Corigliano, M., Lai, C. G., Salazar, W., Scandella, L., Zuccolo, E., Latchman, J., Lynch,
507 L., & Robertson, R., 2011. Probabilistic seismic hazard assessment at the Eastern Caribbean Islands,
508 *Bulletin of the seismological society of America*, **101**(5), 2499–2521, doi: [10.1785/0120100208](https://doi.org/10.1785/0120100208).
- 509 Brune, J. N., 1970. Tectonic stress and the spectra of seismic shear waves from earthquakes, *Journal of*
510 *Geophysical Research*, **75**(26), 4997–5009, doi: [10.1029/JB075i026p04997](https://doi.org/10.1029/JB075i026p04997).
- 511 Bureau de recherches géologiques et minières, 2018. Cartes géologiques imprimées des outre-mer,
512 <https://infoterre.brgm.fr>.
- 513 Castro, R. R., Fabriol, H., Bour, M., & Le Brun, B., 2003. Attenuation and site effects in the region of
514 Guadeloupe, Lesser Antilles, *Bulletin of the Seismological Society of America*, **93**(2), 612–626, doi:
515 [10.1785/0120020042](https://doi.org/10.1785/0120020042).
- 516 Causse, M., Chaljub, E., Cotton, F., Cornou, C., & Bard, P.-Y., 2009. New approach for coupling k^{-2}
517 and empirical Green's functions: application to the blind prediction of broad-band ground motion
518 in the Grenoble basin, *Geophysical Journal International*, **179**(3), 1627–1644, doi: [10.1111/j.1365-](https://doi.org/10.1111/j.1365-246X.2009.04354.x)
519 [246X.2009.04354.x](https://doi.org/246X.2009.04354.x).
- 520 Courboux, F., Converset, J., Balestra, J., & Delouis, B., 2010. Ground-motion simulations of the 2004
521 Mw 6.4 Les Saintes, Guadeloupe, earthquake using ten smaller events, *Bulletin of the Seismological*
522 *Society of America*, **100**(1), 116–130, doi: [10.1785/0120080372](https://doi.org/10.1785/0120080372).
- 523 Davis, R. A., Lii, K.-S., & Politis, D. N., 2011. Remarks on some nonparametric estimates
524 of a density function, in *Selected Works of Murray Rosenblatt*, pp. 95–100, Springer, doi:
525 [10.1214/aoms/1177728190](https://doi.org/10.1214/aoms/1177728190).

- 526 Del Gaudio, S., Causse, M., & Festa, G., 2015. Broad-band strong motion simulations coupling k-
527 square kinematic source models with empirical Green's functions: the 2009 L'Aquila earthquake,
528 *Geophysical Journal International*, **203**(1), 720–736, doi: [10.1093/gji/ggv325](https://doi.org/10.1093/gji/ggv325).
- 529 Del Gaudio, S., Hok, S., Festa, G., Causse, M., & Lancieri, M., 2018. Near-fault broadband ground mo-
530 tion simulations using empirical Green's functions: Application to the Upper Rhine Graben (France–
531 Germany) case study, in *Best Practices in Physics-based Fault Rupture Models for Seismic Hazard
532 Assessment of Nuclear Installations*, pp. 155–177, Springer, doi: [10.1007/s00024-017-1575-1](https://doi.org/10.1007/s00024-017-1575-1).
- 533 DeMets, C., Gordon, R. G., & Argus, D. F., 2010. Geologically current plate motions, *Geophysical
534 Journal International*, **181**(1), 1–80, doi: [10.1111/j.1365-246x.2009.04491.x](https://doi.org/10.1111/j.1365-246x.2009.04491.x).
- 535 Douglas, J., 2003. Earthquake ground motion estimation using strong-motion records: a review of equa-
536 tions for the estimation of peak ground acceleration and response spectral ordinates, *Earth-Science
537 Reviews*, **61**(1-2), 43–104, doi: [10.1016/S0012-8252\(02\)00112-5](https://doi.org/10.1016/S0012-8252(02)00112-5).
- 538 Douglas, J. & Mohais, R., 2009. Comparing predicted and observed ground motions from subduction
539 earthquakes in the Lesser Antilles, *Journal of seismology*, **13**(4), 577–587, doi: [10.1007/s10950-008-
540 9150-y](https://doi.org/10.1007/s10950-008-9150-y).
- 541 Dujardin, A., Causse, M., Courboux, F., & Traversa, P., 2016. Simulation of the basin effects in the Po
542 Plain during the Emilia-Romagna seismic sequence (2012) using empirical Green's functions, *Pure
543 and Applied Geophysics*, **173**(6), 1993–2010, doi: [10.1007/s00024-015-1233-4](https://doi.org/10.1007/s00024-015-1233-4).
- 544 Dziewonski, A. M., Chou, T.-A., & Woodhouse, J. H., 1981. Determination of earthquake source
545 parameters from waveform data for studies of global and regional seismicity, *Journal of Geophysical
546 Research: Solid Earth*, **86**(B4), 2825–2852, doi: [10.1029/jb086ib04p02825](https://doi.org/10.1029/jb086ib04p02825).
- 547 Ekström, G., Nettles, M., & Dziewoński, A., 2012. The global CMT project 2004–2010: Centroid-
548 moment tensors for 13, 017 earthquakes, *Physics of the Earth and Planetary Interiors*, **200-201**, 1–9,
549 doi: [10.1016/j.pepi.2012.04.002](https://doi.org/10.1016/j.pepi.2012.04.002).
- 550 Eshelby, J. D., 1957. The determination of the elastic field of an ellipsoidal inclusion, and related
551 problems, *Proceedings of the Royal Society of London A: Mathematical, Physical and Engineering
552 Sciences*, **241**(1226), 376–396, doi: [10.1098/rspa.1957.0133](https://doi.org/10.1098/rspa.1957.0133).
- 553 Feuillet, N., Beauducel, F., & Tapponnier, P., 2011. Tectonic context of moderate to large historical
554 earthquakes in the Lesser Antilles and mechanical coupling with volcanoes, *Journal of Geophysical
555 Research: Solid Earth*, **116**(B10), doi: [10.1029/2011JB008443](https://doi.org/10.1029/2011JB008443).
- 556 Gallovič, F., 2016. Modeling velocity recordings of the Mw 6.0 South Napa, California, earthquake:
557 Unilateral event with weak high-frequency directivity, *Seismological Research Letters*, **87**(1), 2–14,
558 doi: [10.1785/0220150042](https://doi.org/10.1785/0220150042).
- 559 Ghofrani, H., Atkinson, G. M., & Goda, K., 2013. Implications of the 2011 M9.0 Tohoku Japan earth-
560 quake for the treatment of site effects in large earthquakes, *Bulletin of Earthquake Engineering*, **11**(1),
561 171–203, doi: [10.1007/s10518-012-9413-4](https://doi.org/10.1007/s10518-012-9413-4).
- 562 Hartzell, S., Leeds, A., Frankel, A., Williams, R. A., Odum, J., Stephenson, W., & Silva, W., 2002. Sim-

- 563 ulation of broadband ground motion including nonlinear soil effects for a magnitude 6.5 earthquake
564 on the Seattle fault, Seattle, Washington, *Bulletin of the Seismological Society of America*, **92**(2),
565 831–853, doi: [10.1785/0120010114](https://doi.org/10.1785/0120010114).
- 566 Hartzell, S. H., 1978. Earthquake aftershocks as Green’s functions, *Geophysical Research Letters*, **5**(1),
567 1–4, doi: [10.1029/GL005i001p00001](https://doi.org/10.1029/GL005i001p00001).
- 568 Hunter, J. D., 2007. Matplotlib: A 2D graphics environment, *Computing in Science & Engineering*,
569 **9**(3), 90–95, doi: [10.1109/MCSE.2007.55](https://doi.org/10.1109/MCSE.2007.55).
- 570 Hutchings, L., Ioannidou, E., Foxall, W., Voulgaris, N., Savy, J., Kalogeras, I., Scognamiglio, L., &
571 Stavrakakis, G., 2007. A physically based strong ground-motion prediction methodology; application
572 to PSHA and the 1999 $M_w = 6.0$ Athens earthquake, *Geophysical Journal International*, **168**(2),
573 659–680, doi: [10.1111/j.1365-246X.2006.03178.x](https://doi.org/10.1111/j.1365-246X.2006.03178.x).
- 574 Imperator, W. & Mai, P. M., 2012. Sensitivity of broad-band ground-motion simulations to earthquake
575 source and Earth structure variations: an application to the Messina Straits (Italy), *Geophysical Journal*
576 *International*, **188**(3), 1103–1116, doi: [10.1111/j.1365-246X.2011.05296.x](https://doi.org/10.1111/j.1365-246X.2011.05296.x).
- 577 IPGP, 2008a. Seismic, deformation, gas, magnetic and weather permanent networks on soufrière vol-
578 cano and guadeloupe island, doi: [10.18715/GUADELOUPE.GL](https://doi.org/10.18715/GUADELOUPE.GL).
- 579 IPGP, 2008b. Seismic, deformation, gas, magnetic and weather permanent networks on mount pelée
580 volcano and martinique island, doi: [10.18715/MARTINIQUE.MQ](https://doi.org/10.18715/MARTINIQUE.MQ).
- 581 IPGP, 2008c. Gnss, seismic broadband and strong motion permanent networks in west indies, doi:
582 [10.18715/ANTILLES.WI](https://doi.org/10.18715/ANTILLES.WI).
- 583 IPGP & EOST, 1982. Geoscope, french global network of broad band seismic stations, doi:
584 [10.18715/GEOSCOPE.G](https://doi.org/10.18715/GEOSCOPE.G).
- 585 Irikura, K., 1986. Prediction of strong acceleration motion using empirical Green’s function, in *Proc.*
586 *7th Japan Earthq. Eng. Symp*, vol. 151, pp. 151–156, available from [http://www.kojiro-irikura.](http://www.kojiro-irikura.jp/pdf/7th_J_Earthquake_Eng_Sympo.pdf)
587 [jp/pdf/7th_J_Earthquake_Eng_Sympo.pdf](http://www.kojiro-irikura.jp/pdf/7th_J_Earthquake_Eng_Sympo.pdf).
- 588 Kamae, K. & Irikura, K., 1998. Source model of the 1995 Hyogo-ken Nanbu earthquake and simulation
589 of near-source ground motion, *Bulletin of the Seismological Society of America*, **88**(2), 400–412.
- 590 KNMI, 2006. Caribbean netherlands seismic network, doi: [10.21944/DFFA7A3F-7E3A-3B33-A436-](https://doi.org/10.21944/DFFA7A3F-7E3A-3B33-A436-516A01B6AF3F)
591 [516A01B6AF3F](https://doi.org/10.21944/DFFA7A3F-7E3A-3B33-A436-516A01B6AF3F).
- 592 Kotha, S. R., 2018. *Quantification of uncertainties in seismic ground-motion prediction*, Ph.D.
593 thesis, Universität Potsdam Potsdam, [http://nbn-resolving.de/urn/resolver.pl?urn=urn:](http://nbn-resolving.de/urn/resolver.pl?urn=urn:nbn:de:kobv:517-opus4-415743)
594 [nbn:de:kobv:517-opus4-415743](http://nbn-resolving.de/urn/resolver.pl?urn=urn:nbn:de:kobv:517-opus4-415743).
- 595 Krischer, L., Megies, T., Barsch, R., Beyreuther, M., Lecocq, T., Caudron, C., & Wassermann, J., 2015.
596 ObsPy: a bridge for seismology into the scientific Python ecosystem, *Computational Science & Dis-*
597 *covery*, **8**(1), 014003, doi: [10.1088/1749-4699/8/1/014003](https://doi.org/10.1088/1749-4699/8/1/014003).
- 598 Laigle, M., Hirn, A., Sapin, M., Bécel, A., Charvis, P., Flueh, E., Diaz, J., Lebrun, J.-F., Gesret, A.,
599 Raffaele, R., et al., 2013. Seismic structure and activity of the north-central Lesser Antilles subduction

- 600 zone from an integrated approach: Similarities with the Tohoku forearc, *Tectonophysics*, **603**, 1–20,
 601 doi: [10.1016/j.tecto.2013.05.043](https://doi.org/10.1016/j.tecto.2013.05.043).
- 602 Lancieri, M., Renault, M., Berge-Thierry, C., Gueguen, P., Baumont, D., & Perrault, M., 2015. Strategy
 603 for the selection of input ground motion for inelastic structural response analysis based on naïve
 604 Bayesian classifier, *Bulletin of Earthquake Engineering*, **13**(9), 2517–2546, doi: [10.1007/s10518-015-9728-z](https://doi.org/10.1007/s10518-015-9728-z).
- 605
 606 Madariaga, R. & Ruiz, S., 2016. Earthquake dynamics on circular faults: A review 1970–2015, *Journal*
 607 *of Seismology*, **20**(4), 1235–1252, doi: [10.1007/s10950-016-9590-8](https://doi.org/10.1007/s10950-016-9590-8).
- 608 McGuire, J. & Ben-Zion, Y., 2017. Detailed analysis of earthquake directivity in the San Jacinto Fault
 609 Zone, *SCEC Final Report, Project 16104*, <https://www.scec.org/proposal/report/16104>.
- 610 Oral, E., Gélis, C., & Bonilla, L. F., 2019. 2-D P-SV and SH spectral element modelling of seismic
 611 wave propagation in non-linear media with pore-pressure effects, *Geophysical Journal International*,
 612 **217**(2), 1353–1365, doi: [10.1093/gji/ggz041](https://doi.org/10.1093/gji/ggz041).
- 613 OVSG & OVSM, 2020. Unified seismic catalogue for the Lesser Antilles, 2014-2019, doi:
 614 [10.18715/IPGP.2020.kgmbivor](https://doi.org/10.18715/IPGP.2020.kgmbivor).
- 615 Pacor, F., Ameri, G., Galovic, F., & D'Amico, M., 2017. Ground motion variability from finite fault
 616 simulations, in *Proceedings of the 16th World Conference on Earthquake (16WCEE), Santiago, Chile*,
 617 pp. 9–13.
- 618 Parzen, E., 1962. On estimation of a probability density function and model, *Annals of Mathematical*
 619 *Statistics*, **33**(3), 1065–1076, doi: [10.1214/aoms/1177704472](https://doi.org/10.1214/aoms/1177704472).
- 620 Paulatto, M., Laigle, M., Galve, A., Charvis, P., Sapin, M., Bayrakci, G., Evain, M., & Kopp, H., 2017.
 621 Dehydration of subducting slow-spread oceanic lithosphere in the Lesser Antilles, *Nature communi-*
 622 *cations*, **8**, 15980, doi: [10.1038/ncomms15980](https://doi.org/10.1038/ncomms15980).
- 623 Pavic, R., Koller, M. G., Bard, P.-Y., & Lacave-Lachet, C., 2000. Ground motion prediction with the
 624 empirical Green's function technique: an assessment of uncertainties and confidence level, *Journal of*
 625 *Seismology*, **4**(1), 59–77, doi: [10.1023/A:1009826529269](https://doi.org/10.1023/A:1009826529269).
- 626 Pulido, N., Ojeda, A., Atakan, K., & Kubo, T., 2004. Strong ground motion estimation in the Sea of
 627 Marmara region (Turkey) based on a scenario earthquake, *Tectonophysics*, **391**(1-4), 357–374, doi:
 628 [10.1016/j.tecto.2004.07.023](https://doi.org/10.1016/j.tecto.2004.07.023).
- 629 Ragon, T., Sladen, A., & Simons, M., 2019. Accounting for uncertain fault geometry in earthquake
 630 source inversions—II: application to the M_w 6.2 Amatrice earthquake, central Italy, *Geophysical Jour-*
 631 *nal International*, **218**(1), 689–707, doi: [10.1093/gji/ggz180](https://doi.org/10.1093/gji/ggz180).
- 632 Régnier, J., Cadet, H., Bonilla, L. F., Bertrand, E., & Semblat, J.-F., 2013. Assessing nonlinear behavior
 633 of soils in seismic site response: Statistical analysis on KiK-net strong-motion data, *Bulletin of the*
 634 *Seismological Society of America*, **103**(3), 1750–1770, doi: [10.1785/0120120240](https://doi.org/10.1785/0120120240).
- 635 Ripperger, J., Mai, P., & Ampuero, J.-P., 2008. Variability of near-field ground motion from dynamic
 636 earthquake rupture simulations, *Bulletin of the seismological society of America*, **98**(3), 1207–1228,

- 637 doi: [10.1785/0120070076](https://doi.org/10.1785/0120070076).
- 638 Ruiz, J., Baumont, D., Bernard, P., & Berge-Thierry, C., 2011. Modelling directivity of strong ground
639 motion with a fractal, k^{-2} , kinematic source model, *Geophysical Journal International*, **186**(1), 226–
640 244, doi: [10.1111/j.1365-246X.2011.05000.x](https://doi.org/10.1111/j.1365-246X.2011.05000.x).
- 641 Ruiz, M., Galve, A., Monfret, T., Sapin, M., Charvis, P., Laigle, M., Evain, M., Hirn, A., Flueh, E.,
642 Gallart, J., et al., 2013. Seismic activity offshore Martinique and Dominica islands (Central Lesser
643 Antilles subduction zone) from temporary onshore and offshore seismic networks, *Tectonophysics*,
644 **603**, 68–78, doi: [10.1016/j.tecto.2011.08.006](https://doi.org/10.1016/j.tecto.2011.08.006).
- 645 Russo, R. M., Okal, E. A., & Rowley, K. C., 1992. Historical seismicity of the southeastern Caribbean
646 and tectonic implications, *Pure and Applied Geophysics*, **139**(1), 87–120, doi: [10.1007/BF00876827](https://doi.org/10.1007/BF00876827).
- 647 Satriano, C., 2020. SourceSpec – Earthquake source parameters from S-wave displacement spectra,
648 doi: [10.5281/ZENODO.3688587](https://doi.org/10.5281/ZENODO.3688587).
- 649 Satriano, C., Dionicio, V., Miyake, H., Uchida, N., Vilotte, J.-P., & Bernard, P., 2014. Structural and
650 thermal control of seismic activity and megathrust rupture dynamics in subduction zones: Lessons
651 from the Mw 9.0, 2011 Tohoku earthquake, *Earth and Planetary Science Letters*, **403**, 287–298, doi:
652 [10.1016/j.epsl.2014.06.037](https://doi.org/10.1016/j.epsl.2014.06.037).
- 653 Sørensen, M. B., Pulido, N., & Atakan, K., 2007. Sensitivity of ground-motion simulations to earth-
654 quake source parameters: a case study for Istanbul, Turkey, *Bulletin of the Seismological Society of*
655 *America*, **97**(3), 881–900, doi: [10.1785/0120060044](https://doi.org/10.1785/0120060044).
- 656 Spudich, P., Cirella, A., Scognamiglio, L., & Tinti, E., 2019. Variability in synthetic earthquake ground
657 motions caused by source variability and errors in wave propagation models, *Geophysical Journal*
658 *International*, **219**(1), 346–372, doi: [10.1093/gji/ggz275](https://doi.org/10.1093/gji/ggz275).
- 659 Vallée, M., Charléty, J., Ferreira, A. M., Delouis, B., & Vergoz, J., 2011. SCARDEC: a new technique
660 for the rapid determination of seismic moment magnitude, focal mechanism and source time functions
661 for large earthquakes using body-wave deconvolution, *Geophysical Journal International*, **184**(1),
662 338–358, doi: [10.1111/j.1365-246X.2010.04836.x](https://doi.org/10.1111/j.1365-246X.2010.04836.x).
- 663 Wang, H., Igel, H., Gallovič, F., & Cochard, A., 2009. Source and basin effects on rotational ground
664 motions: Comparison with translations, *Bulletin of the Seismological Society of America*, **99**(2B),
665 1162–1173, doi: [10.1785/0120080115](https://doi.org/10.1785/0120080115).
- 666 Weil-Accardo, J., Feuillet, N., Jacques, E., Deschamps, P., Beauducel, F., Cabioch, G., Tapponnier, P.,
667 Saurel, J.-M., & Galetzka, J., 2016. Two hundred thirty years of relative sea level changes due to
668 climate and megathrust tectonics recorded in coral microatolls of Martinique (French West Indies),
669 *Journal of Geophysical Research: Solid Earth*, **121**(4), 2873–2903, doi: [10.1002/2015JB012406](https://doi.org/10.1002/2015JB012406).
- 670 Wessel, P., Luis, J. F., Uieda, L., Scharroo, R., Wobbe, F., Smith, W. H. F., & Tian, D., 2019. The
671 Generic Mapping Tools Version 6, *Geochemistry, Geophysics, Geosystems*, **20**(11), 5556–5564, doi:
672 [10.1029/2019gc008515](https://doi.org/10.1029/2019gc008515).
- 673 Withers, K. B., Olsen, K. B., Shi, Z., & Day, S. M., 2019. Validation of Deterministic Broadband

- 674 Ground Motion and Variability from Dynamic Rupture Simulations of Buried Thrust Earthquakes
675 Validation of Deterministic Broadband Ground Motion and Variability, *Bulletin of the Seismological*
676 *Society of America*, **109**(1), 212–228, doi: [10.1785/0120180005](https://doi.org/10.1785/0120180005).
- 677 Zhao, J. X., Zhang, J., Asano, A., Ohno, Y., Oouchi, T., Takahashi, T., Ogawa, H., Irikura, K., Thio,
678 H. K., Somerville, P. G., et al., 2006. Attenuation relations of strong ground motion in Japan using site
679 classification based on predominant period, *Bulletin of the Seismological Society of America*, **96**(3),
680 898–913, doi: [10.1785/0120050122](https://doi.org/10.1785/0120050122).